Journal of Marine Research, 51, 109–134, 1993

Steady wind forcing of a density front over a circular bank

by Glen Gawarkiewicz[1]

ABSTRACT

The response of a density front along the edge of a circular bank to steady wind forcing is examined using a primitive equation numerical model. Initially, the fluid is at rest with relatively light, vertically homogeneous water over the bank. The density field is allowed to adjust geostrophically and frictionally for ten days, after which a spatially uniform wind stress is applied for three days. The resulting surface velocity field over the bank is asymmetrical, with a relative maximum on the downwind side of the bank to the left of the wind direction and a relative minimum on the upwind side of the bank to the right of the wind direction. For the small Ekman number considered here, the density-driven flow persists beneath the surface Ekman layer. Light fluid is advected off the bank near the surface in the direction of Ekman transport, weakening the surface density gradients. On the opposite side of the bank, the vertical structure of the density field is weakened and the surface density gradients remain relatively constant. When the wind stress is abruptly turned off, the anti-cyclonic surface velocity is restored within one inertial period, and some light fluid remains off the bank. The loss of neutrally buoyant near-surface particles released over the bank primarily occurs from the region of the bank downwind and to the right. The presence of the density front slightly increases the number of particles lost from the bank. A simple formula for the particle loss is presented.

1. Introduction

Submarine banks are among the most biologically productive regions in the oceans. For example, the Grand Banks and Georges Bank in the North Atlantic Ocean have ecosystems which support large fisheries. However, the recruitment of commercially important fish species such as cod and haddock to the bank ecosystems is subject to large inter-annual variability (e.g. GLOBEC, 1992), and understanding the causes of the variability has been a persistent theme of many investigators. A particularly important aspect of this problem is the role of off-bank advection and exchange of bank water and plankton into the adjacent water masses. For example, in the models of Walsh *et al.* (1987) and Klein (1987), the level of bank productivity was sensitive to the parameter representing the horizontal diffusion and loss from the bank. In each of these models, the parameter representing horizontal exchange was a long-term seasonal average lumping together many wind-induced and eddy-induced events.

1. Woods Hole Oceanographic Institution, Woods Hole, Massachusetts, 02543, U.S.A.

Advection and exchange processes between submarine banks and the adjacent water masses are complicated by several factors. The mean circulation over many banks is a combination of density-driven, wind-driven, and tidal residual flows (Loder *et al.,* 1988). There may be pronounced seasonal differences in the mean flow and stratification over submarine banks due to seasonal variations in surface and lateral buoyancy inputs. Vertical mixing processes due to tidal and wind forcing and the behavior of the bottom and surface boundary layers are affected by a wide variety of high-frequency processes and are not well understood. The presence of density fronts at the edge of many banks leads to complex, three-dimensional flow patterns within the frontal regions.

The response of density fronts to wind forcing has been studied by many investigators along straight continental shelves (e.g. Csanady, 1978, 1984; Ou, 1984a; Ikeda, 1985; Chao, 1988), but the response of a bank-trapped density front to wind forcing has not been considered, and is the subject of this study. Two important questions will be addressed. First, does the presence of a density front at the edge of a bank inhibit the loss of water from the bank due to wind forcing? Second, what are the spatial patterns of the advective losses from an idealized circular bank due to wind forcing, and how are they affected by the presence of the density front and the associated thermohaline circulation?

The interaction of the velocity field with the density field in the frontal region is inherently nonlinear, so the semi-spectral primitive equation model (SPEM) of Haidvogel *et al.* (1991) is used to address these questions. In order to keep the setting as simple as possible, idealized topography is used and the initial density front is formed by the geostrophic adjustment of light fluid centered over the bank (Section 3). Simple representations of the vertical mixing are assumed. The response of the density front encircling the bank to moderate and strong wind forcing is described in Section 4, followed in Section 5 by the response to abrupt cessation of wind forcing. The trajectories of neutrally buoyant particles appear in Section 6. The results are discussed in Section 7, with conclusions appearing in Section 8.

2. The numerical model

The semi-spectral primitive equation model (SPEM) of Haidvogel *et al.* (1991) is hydrostatic, Boussinesq, and assumes a rigid lid at the surface. The model employs a sigma (topography-following) coordinate system. A complete description of the model is provided by Hedstrom (1990).

The momentum and continuity equations are, with subscripts denoting partial differentiation,

$$u_t + (uu_x + vu_y + wu_z) - fv = -\frac{1}{\rho_0}p_x + (A_V u_z)_z + F_u \tag{1}$$

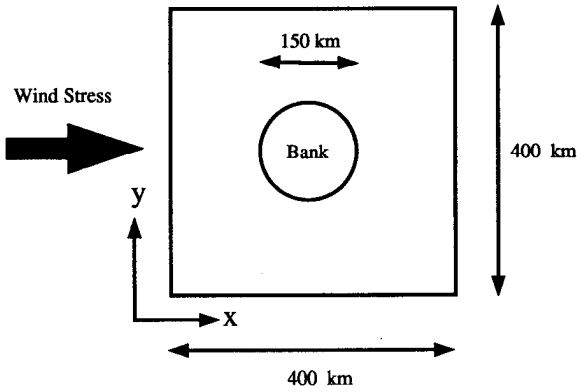

Figure 1. A plan view of the model domain. The horizontal extent is 400 × 400 km. A submarine bank with a radius of 75 km is present in the center of the domain. The spatially-uniform steady wind stress is applied in the positive x direction.

$$v_t + (uv_x + vv_y + wv_z) + fu = -\frac{1}{\rho_0}p_y + (A_V v_z)_z + F_v \tag{2}$$

$$u_x + v_y + w_z = 0 \tag{3}$$

$$p_z = -\rho g \tag{4}$$

where A_v is the vertical eddy viscosity and F_u, F_v are lateral mixing terms applied along sigma-coordinate surfaces and used for numerical stability. A bi-harmonic operator is used for F_u, F_v, with a mixing coefficient of 5×10^9 m^4 s^{-1}. The x and y directions are defined in Figure 1; in the cases in Section 4 with wind forcing the wind stress will always be applied in the $+x$ direction. The vertical coordinate is z, and is defined positive upward with the origin located at the (rigid) surface. Variables u, v, and w are the velocities in the x, y, and z directions. The time is denoted by t, and the pressure by p. The mean density is $\rho_0 = 1000$ kg m^{-3} throughout.

The equation for the density field is

$$\rho_t + u\rho_x + v\rho_y + w\rho_z = (K_V\rho_z)_z \tag{5}$$

where ρ is the density deviation from the reference density ρ_0, K_v is the vertical eddy diffusivity, and there is no horizontal mixing of density. A scheme to insure that static stability is maintained throughout the water column is also used in the model.

The model employs an Arakawa C grid with finite differences in the horizontal and a spectral expansion in modified Chebyshev polynomials in the vertical. The collocation points in the vertical correspond to the extrema of the Chebyshev polynomials and are distributed according to the relation

$$\sigma_n = \cos\left(\frac{\pi(n-N)}{N}\right) \quad \text{for } n = 0, N \tag{6}$$

where σ_n is the non-dimensional vertical coordinate such that ($\sigma = 1 + (2z/h)$), N is the number of Chebyshev polynomials used in the expansion, and h is the depth of the bottom. The collocation points are thus concentrated near the surface and bottom boundaries with a minimum spacing of 1.2 m at the center of the bank adjacent to the surface and bottom boundaries ($h = 50$ m with $N = 10$) and 6.1 m in the deepest portion of the model domain ($h = 250$ m with $N = 10$). The mixing coefficients are assumed constant with $A_v = K_v = 0.005$ m^2 s^{-1}.

The surface boundary conditions are

$$A_V u_z = \tau_x/\rho_o, A_V v_z = \tau_y/\rho_o \quad \text{at } z = 0 \tag{7}$$

where τ_x and τ_y are the x and y components of the wind stress. For the first ten days of model time, both τ_x and τ_y are set to zero during geostrophic adjustment (Section 3). For days 10–13, τ_x is set to a constant value and τ_y remains zero (Section 4). For days 13–16, the wind stress is abruptly turned off with τ_x and τ_y set to zero (Section 5). Surface density (heat) flux is neglected in all cases, i.e.

$$\rho_z = 0 \quad \text{at } z = 0. \tag{8}$$

Linear bottom friction is used

$$A_V u_z = -\gamma u, A_V v_z = -\gamma v \quad \text{at } z = -h \tag{9}$$

with $\gamma = 5. \times 10^{-4}$ m s^{-1} for most of the runs. A no-flux condition is applied on density at the bottom.

The model domain is sketched in Figure 1. A circular bank with a 75 km radius is placed in the middle of a square 400 km × 400 km computational domain. The fluid depth is

$$h(r) = \begin{cases} 50. + 0.00067r & \text{for } r < 75 \text{ km} \\ 100. + 0.03(r - 75 \text{ km}) & \text{for } 75 \text{ km} < r < 80 \text{ km} \\ 250. & \text{for } r > 80 \text{ km} \end{cases}$$

where h and r are in units of meters, and r is the radial distance from the center of the bank (i.e. $r = \sqrt{(x - 200 \text{ km})^2 + (y - 200 \text{ km})^2}$). Two separate boundary conditions were used for the outer boundaries. For most runs, the four boundaries were solid (i.e. no normal flow) and free-slip. This approach is simple but has the disadvantage of generating return flows from the wind-driven circulation due to set-up along the boundaries, and so several runs were performed using a periodic channel oriented in the direction of the Ekman transport. No significant differences were evident for wind forcing of 5 days or less. The lateral boundaries also allow Kelvin waves to propagate around the domain but these waves did not interact with the bank flow in the cases described here.

A 97 × 97 horizontal grid (4.2 km resolution) was used. Comparison with a model

run with a 3.3 km grid resolution revealed only minor differences. Eleven Chebyshev polynomials were used ($N = 10$) after tests with thirteen polynomials showed very similar results. The time step for most of the runs was 108 s with slight variations when different vertical mixing coefficients were used. In all cases, the rotation rate was uniform with $f = 10^{-4}\ s^{-1}$.

3. Geostrophic adjustment

The first step in determining the joint effects of the thermohaline circulation and the wind-induced circulation on advective losses from the bank is to establish the unforced thermohaline circulation. In this section, an initially motionless fluid with a prescribed density distribution is allowed to adjust geostrophically to a quasi-steady state in which the velocity and density fields are in balance. Similar problems have been examined along a straight, two-dimensional (no along-shelf variation) continental shelf by Ou (1983, 1984b) for a two-layer fluid over step topography, and by Wang (1984) for a continuously stratified fluid over sloping topography. Dewar and Killworth (1990) have studied the adjustment of a cylinder of dense fluid over a flat bottom using a two-layer inviscid model. The fundamental dynamics in all these cases are the same as that described next.

The transient response is limited by the lack of initial vertical stratification in the region exterior to the bank which precludes the propagation of internal waves away from the bank. Similarly, the use of a rigid lid removes high frequency surface gravity waves. Processes associated with non-hydrostatic effects such as wave breaking (Killworth, 1992) are also absent from the model. Thus the only transient motions present in this system are inertial frontal waves.

At time $t = 0$, vertically uniform light ($\rho = 0.0\ kg\ m^{-3}$) fluid is centered over the bank with a radius of 55 km. Over the interval 55 km $\leq r \leq$ 75 km, ρ increases linearly from 0.0 kg m^{-3} to 0.5 kg m^{-3}, and is a constant $\rho = 0.5\ kg\ m^{-3}$ everywhere for $r \geq 75$ km. The initial phase of the adjustment process, $t \ll f^{-1}$, is dominated by the radial acceleration of the near-bottom velocity field onto the bank in response to the initially unbalanced pressure field. This initial inward radial flow along the bottom is balanced by a radial outflow at the surface. Large upward (downward) velocities are present at the inner (outer) edge of the density gradient region.

For $t \approx f^{-1}$, the inertial time scale, the influence of rotation deflects the radial currents to the right, and thus a cyclonic flow develops near the bottom and an anti-cyclonic flow develops near the surface. The primary balance in the radial momentum equation is inertial and the azimuthal velocity continues to grow at both the surface and bottom until the radial flow ceases to accelerate, at which point inertial motions propagate through the density gradient region. These inertial transients are dissipated by the vertical diffusion, and are damped after roughly 5 days. For $t \gg f^{-1}$, the flow reaches a quasi-steady state in which the temporal changes in the velocity field are due only to vertical diffusive processes.

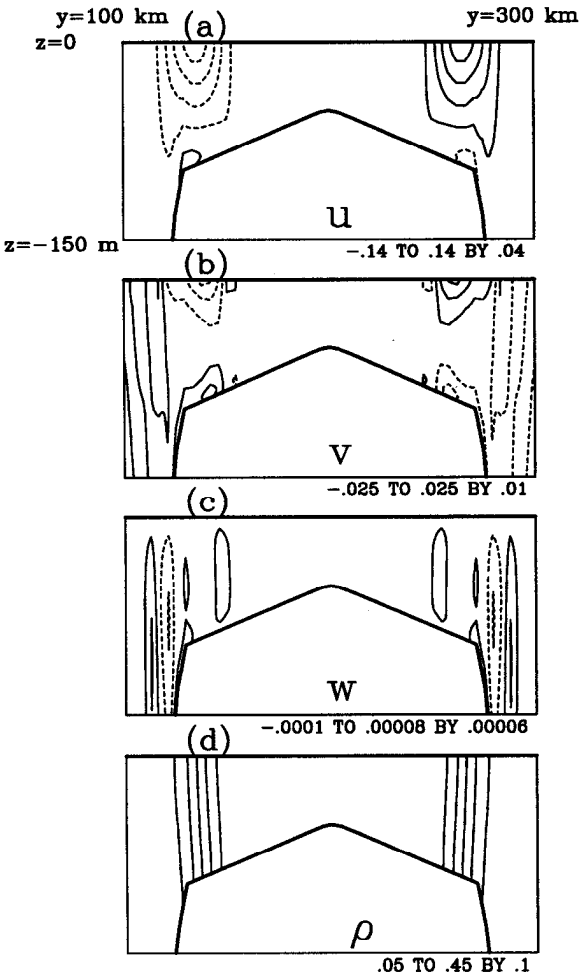

Figure 2. Cross-channel slices at x = 200 km of (a) the u (azimuthal) velocity, (b) the v (radial) velocity, (c) the vertical velocity w, and (d) the density after 10 days of geostrophic adjustment. Positive values denote flow out of the page in (a), to the right of the figure in (b), and upwards in (c). The contour values are in units of m s^{-1} except in (d), which is in kg m^{-3}. In all vertical slices, only the upper 150 m of the water column is shown although the model domain extends to 250 m.

The velocity fields and density field for t = 10 days are shown in Figure 2. The azimuthal velocity field (u) is anti-cyclonic at the surface and reaches a maximum of 0.19 m s^{-1} at r = 75 km (Fig. 2a). This gives a time scale of 29 days for a particle to circle the bank. Bottom friction acts to decelerate the near-bottom flow, but remnants of the cyclonic near-bottom flow are present. The maximum azimuthal

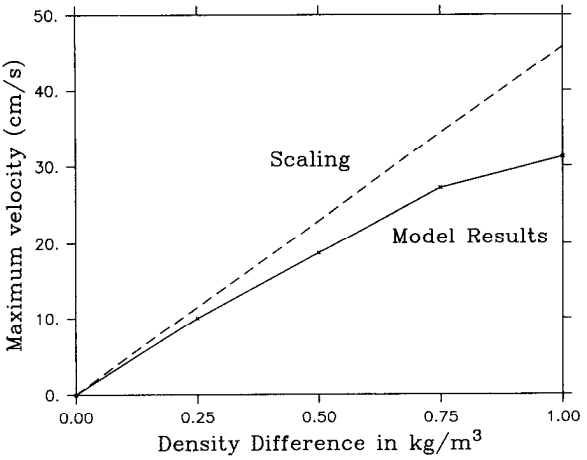

Figure 3. The maximum azimuthal surface velocity as a function of initial density difference ($\Delta\rho$) across the density gradient region. The solid line shows the model values. The dashed line is the scaling in Eq. (10).

velocity can be estimated from geostrophy and the hydrostatic relation as

$$u_b \approx \frac{1}{f\rho_o}\frac{\partial p}{\partial r} \approx \frac{H}{f\rho_o}\frac{g\Delta\rho}{L_w} \tag{10}$$

where H is the depth of the bank in the density gradient region, $\Delta\rho$ is the horizontal density difference, and L_w is the initial width of the density gradient region. This scaling compares favorably with the model velocities (Fig. 3) as a function of $\Delta\rho$, although (10) slightly overestimates the maximum azimuthal velocity.

Upon reaching the quasi-steady state depicted in Figure 3, the vertical diffusion is relatively unimportant except locally at the upper and lower boundaries within the density gradient region. That is, the Ekman number is small,

$$E_V = \frac{2A_V}{fH^2} = 0.04 \tag{11}$$

(with $H = 50$ m, $A_v = 0.005$ m^2 s^{-1}). Similarly, the nonlinear momentum terms are unimportant compared to the rotation term, i.e. the Rossby number is small

$$R_O = \frac{u}{fL} = 0.03 \tag{12}$$

where $u = 0.2$ m s^{-1} and $L = 75$ km.

The radial velocity field (v) is weaker than the azimuthal velocity field by roughly an order of magnitude, with maximum velocities of 0.025 m s^{-1} outward near the surface and slightly smaller velocities inward near the bottom at the edge of the bank

(Fig. 2b). The vertical velocity field is dominated by an upward cell near $r = 55$ km, with a maximum velocity of 4×10^{-5} m s^{-1}, and a downward cell near $r = 75$ km, with a maximum velocity of -1.0×10^{-4} m s^{-1} (Fig. 2c). The isopycnals spread slightly near the surface and become more horizontal, consistent with the release of available potential energy, although this is not easily seen in Figure 2d because of the large horizontal scales.

For the limited parameter range described here, the azimuthal flow is stable for all cases, i.e. baroclinic instabilities do not develop within 30 days. While it is beyond the scope of this paper to examine the full parameter space, it is useful to briefly categorize the effects of varying some of the important parameters. Increasing the bottom friction coefficient γ from 5.0×10^{-4} m s^{-1} to 2.5×10^{-3} m s^{-1} inhibits the cyclonic near-bottom flow, decreasing from a maximum of 0.015 m s^{-1} for the case previously described to 0.002 m s^{-1}. Increasing the vertical mixing coefficients to 0.01 m^2 s^{-1} has little effect on the anti-cyclonic surface velocities but decreases the maximum radial near-bottom velocity from 0.025 m s^{-1} to 0.01 m s^{-1}. In addition, the inertial oscillations are damped after only two days. Decreasing the vertical mixing coefficients to 0.0025 m^2 s^{-1} increases the radial near-bottom velocity while the surface velocities are again virtually unchanged.

An additional run was performed to ensure that the downward vertical velocities near the edge of the bank were not generated by the steep topography. This was tested by moving the linear density gradient region to 35 km $\leq r \leq$ 55 km. No vertical motions were present for $r > 60$ km, and the transverse cells described previously were present over mid-bank, with the vertical velocities roughly half as large as in the previous case. Thus, the circulation pattern described above is quite robust.

4. Steady wind forcing

In this section, the response of the bank-trapped density and velocity fields described in the previous section to steady, spatially uniform wind forcing is examined. The resulting flow field is primarily a linear superposition of the wind-driven flow, which is to the right of the wind direction at the surface, and the around-bank buoyancy-driven flow (Fig. 4). The only significant nonlinear effect is due to the advection of the density field by the wind-driven flow. Therefore, an important measure of the bank response is the ratio of the maximum wind-driven velocity at the surface to the maximum buoyancy-driven velocity, which for this case is also at the surface. From classical Ekman dynamics, the maximum wind-driven velocity at the surface is

$$u_w = \frac{\sqrt{2}\tau_x}{\rho_o f \delta_E} \tag{13}$$

where $\delta_E = \sqrt{2A_v/f}$ is the Ekman decay scale, which is 10 m for the cases described in

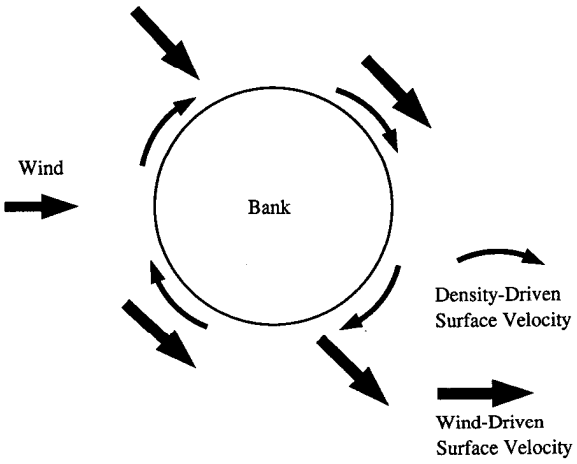

Figure 4. A schematic plan view of the superposition of an Ekman layer surface velocity with an anti-cyclonic surface flow around the bank. The combined flow is a maximum on the downwind side of the bank, at an angle of 45 degrees to the left of the wind direction. The combined flow is a minimum on the upwind side of the bank, 135 degrees to the right of the wind direction. A stagnation point would occur here if the flows were of equal magnitude.

this section. The ratio u_w/u_b, where u_b is the maximum buoyancy-driven velocity at the surface, from (10), indicates whether the wind-driven or buoyancy-driven contributions to the velocity field dominate.

Two magnitudes of wind forcing are considered, $\tau_x = 1$ and 4 dynes cm^{-2}. In each case, the wind stress is spatially uniform over the entire model domain and is impulsively started and held constant for three days. These stresses are roughly equivalent to wind velocities of 7 and 14 m s^{-1} and give values of the ratio u_w/u_b of 0.74 and 3.0.

The surface velocity field for the weaker wind stress ($\tau_x = 1$ dyne cm^{-2}, Fig. 5a) shows a spatial structure similar to the schematic in Figure 4. The velocity field around the edge of the bank is asymmetrical due to the changing orientation of the density-driven flow relative to the wind-driven flow. The magnitude and location of the maximum and minimum velocities are close to those expected through simple linear superposition. For this case, $u_w = 0.14$ m s^{-1}, while $u_b = 0.19$ m s^{-1}, and the maximum surface velocity is 0.34 m s^{-1}, nearly the sum of the two (point B). The minimum surface velocity is 0.005 m s^{-1} (point A) which is less than the value expected from linear superposition due to the advective weakening of surface density gradients.

The surface velocity field resulting from a stronger wind stress ($\tau_x = 4$ dynes cm^{-2}) appears more spatially uniform because of the dominance of the wind-driven velocity field over the density-driven velocity field (Fig. 5b). However, there is still an enhancement of the flow where the two components are aligned and a relative minimum, although not a stagnant region, where the two components are opposed.

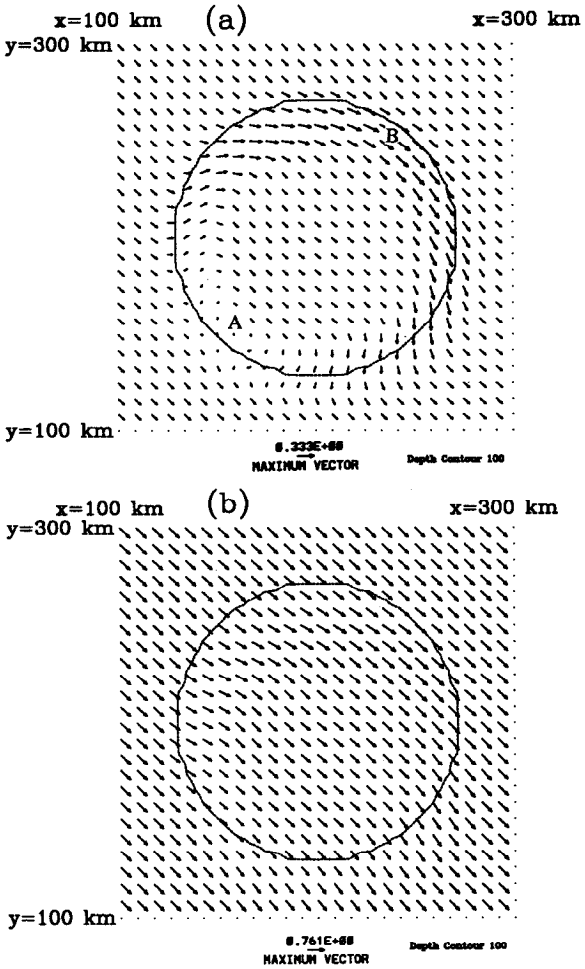

Figure 5. A plan view of the surface velocity field after 3 days of applied wind stress for (a) moderate wind forcing (τ_x = 1 dyne cm^{-2}) and (b) strong wind forcing (τ_x = 4 dynes cm^{-2}). The points A and B in (a) mark the minimum and maximum surface velocities.

The vertical structure of u in the plane perpendicular to the wind direction (along x = 200 km and looking into the wind) appears in Figure 6 for both moderate and strong wind forcing. The wind-driven flow is concentrated in the upper 10 m of the water column. The Ekman transport is onto the bank on the right side of the bank in Figure 6 (i.e. the Ekman transport is in the $-y$ direction), and this region will henceforth be referred to as the "Ekman gain" region of the bank. Here, the wind-driven velocity is partially aligned with the density-driven velocity and there is a relative maximum in the around-bank flow at the surface. On the opposite side of the bank, in the "Ekman loss" region, the density-driven flow is partially opposed to the

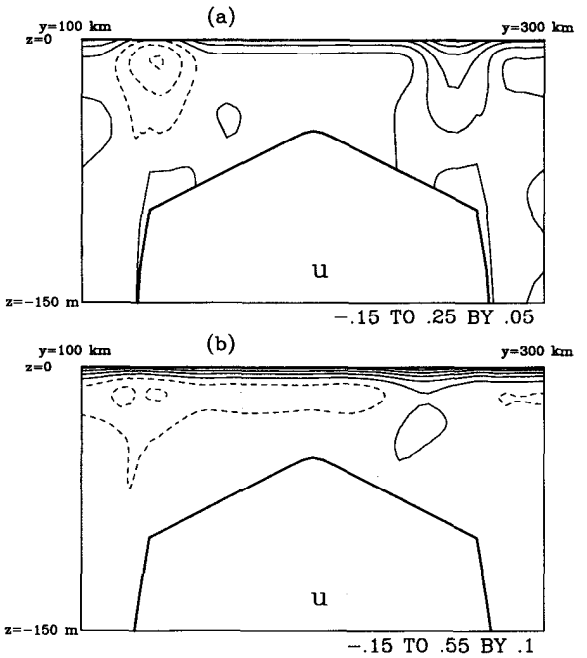

Figure 6. The u velocity at x = 200 km for (a) moderate wind forcing and (b) strong wind forcing. Positive values denote flow out of the page, and the wind direction is out of the page. The contour values are in units of m s^{-1}.

wind-driven flow and there is a sub-surface maximum in the around-bank flow. The density-driven flow is relatively undisturbed at depths greater than δ_E = 10 m. This is consistent with the result of Brink (1983) that Ekman transport across a bank is not affected by bottom topography unless δ_E is comparable to the water depth. For the stronger wind stress (Fig. 6b), the surface flow on the Ekman loss side of the bank actually reverses relative to the initial anti-cyclonic flow. However, the along-bank flow continues at depths beneath δ_E, although it is weaker than in the other case.

The across-bank velocity v is dominated by the wind-driven flow near the surface (Fig. 7). The maximum surface velocities are roughly 0.10 m s^{-1} with τ_x = 1 dyne cm^{-2} (Fig. 7a) and 0.45 m s^{-2} with τ_x = 4 dynes cm^{-2} (Fig. 7b) and are much larger than the radial velocities associated with the density-driven flow alone (Fig. 2b).

The vertical velocity field is quite similar to that of Figure 2c, however, the downward vertical velocity cell at the edge of the bank does not extend into the Ekman layer near the surface. There are no strong convergences or divergences near the surface over the bank because of the spatially uniform wind field.

The wind forcing induces an asymmetry in the surface density field around the bank which is barely evident for moderate wind forcing (Fig. 8a), but pronounced for strong wind forcing (Fig. 8b). Water is advected off the bank from the Ekman loss

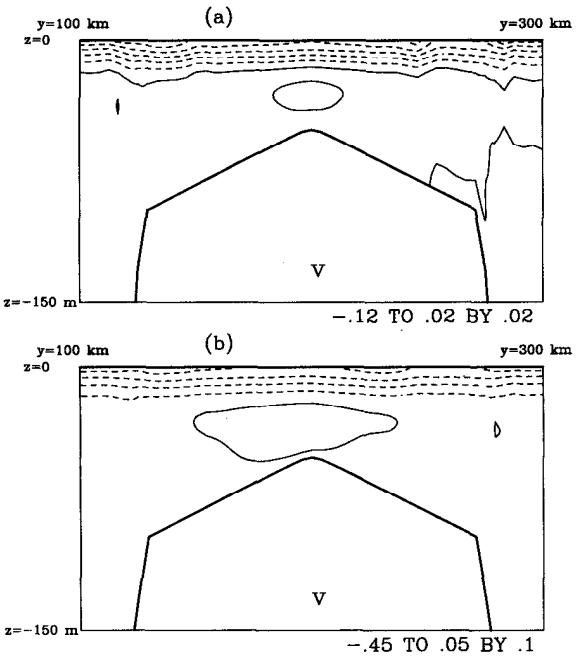

Figure 7. The v velocity at x = 200 km for (a) moderate wind forcing and (b) strong wind forcing. Positive values denote flow to the right in this figure, and the wind direction is out of the page. The contour values are in units of m s^{-1}.

region in the direction ($-y$) of the Ekman transport, while water is advected onto the bank in the Ekman gain region. As a result, the surface density gradients move laterally and weaken, particularly on the Ekman loss side of the bank (Fig. 9), where the maximum surface density gradient decreases by 12% and 56% for moderate and strong wind forcing, respectively. On the Ekman gain side of the bank, the maximum surface density gradient does not decrease substantially.

The vertical structure of the density field (Fig. 10) clearly shows the off-bank advection of light water near the surface on the Ekman loss side of the bank, which is far more pronounced for strong wind forcing. For each case, convective mixing removes the vertical structure in the density field on the Ekman gain side of the bank.

The weakening of the density gradients on the Ekman loss side of the bank implies a weakening of the density-driven flow there. This suggests that the surface flow on the Ekman loss side of the bank would be closer to the wind-driven velocity than the simple superposition of the initial wind-driven and density-driven fields would imply. On the Ekman gain side of the bank, the density gradient changes very little from the geostrophically-adjusted flow, and thus the surface velocity should be close to the sum of the two velocities. These features were mentioned with regard to Figure 5 and can be clearly seen in Figure 11, in which the surface velocity for moderate wind

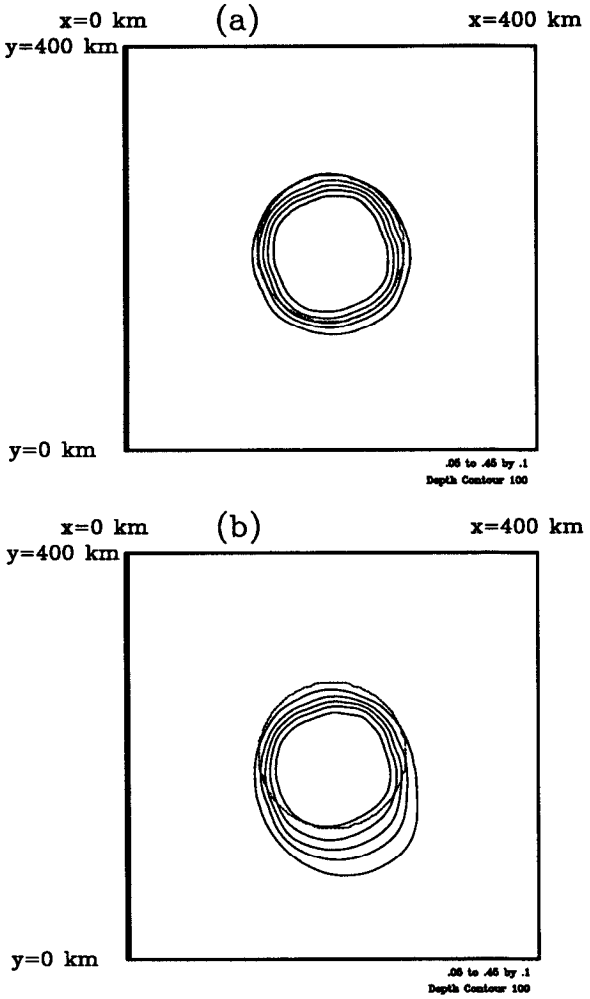

Figure 8. A plan view of the surface perturbation density field after 3 days of strong wind forcing. The wind stress is applied in the $+x$ direction. The edge of the bank (r = 75 km) is indicated by the dotted line. The contour values are in units of kg m^{-3}.

forcing (solid curve) is compared with the superposition of the wind-driven and density-driven velocities (dashed curve). In this figure, the horizontal distance is measured along the diagonal from $x = 0, y = 0$ to $x = 400$ km, $y = 400$ km, and the center of the bank is at 280 km. Points A and B in Figure 5a are near 210 km and 350 km, respectively. The difference between the two curves on the Ekman-loss side of the bank is due to the weakening of the near-surface density gradients caused by wind-driven advection.

The momentum balances are relatively simple. Figure 12 shows the dominant

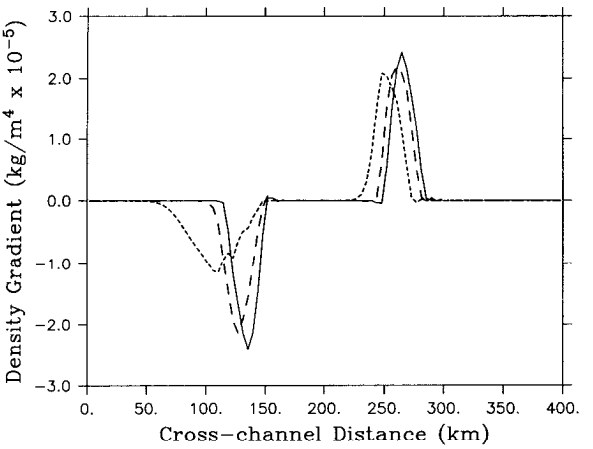

Figure 9. The surface density gradient along x = 200 km after 10 days of geostrophic adjustment (solid line), after 3 days of moderate wind forcing (wide dashed line), and after 3 days of strong wind forcing (narrow dashed line).

terms in the x momentum balance in the plane normal to the wind direction for moderate wind forcing. Near the surface, the classical Ekman balance between diffusion and rotation is dominant everywhere except in the density gradient region, where the pressure gradient is also important. Beneath the Ekman layer the balance

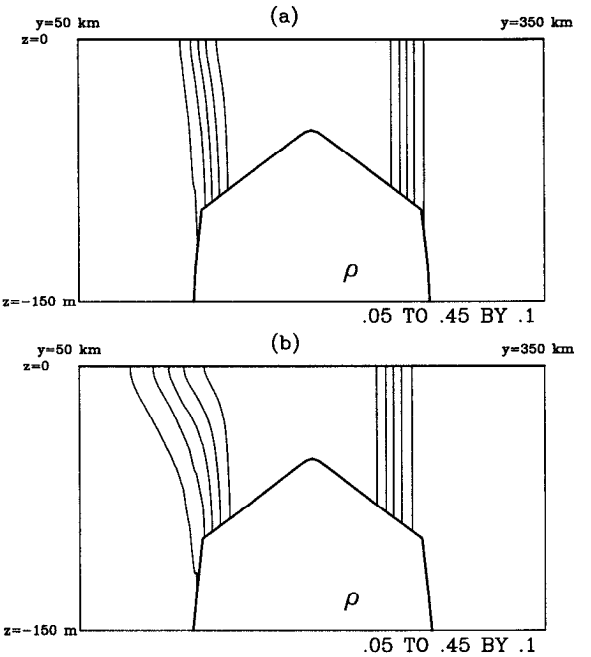

Figure 10. A vertical section of the perturbation density field along x = 200 km after 3 days of wind forcing for (a) moderate wind forcing and (b) strong wind forcing.

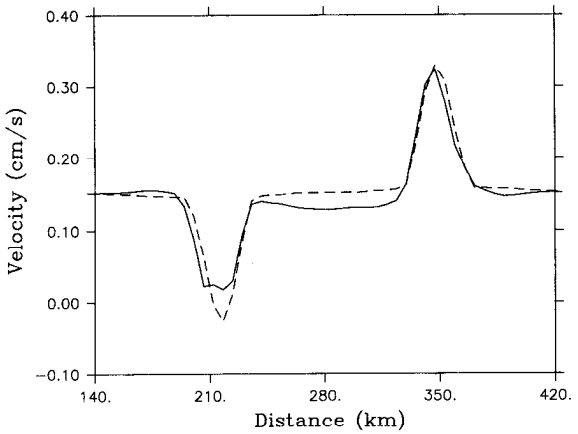

Figure 11. The magnitude of the surface velocity after 3 days of moderate wind forcing (1 dyne cm^{-2}, solid line) as a function of the distance along the diagonal from $x = 0, y = 0$ to $x = 400$ km, $y = 400$ km. The center of the bank corresponds to 280 km in this figure. The linear superposition of the purely geostrophically-adjusted flow plus the purely wind-driven flow appears as the dashed line.

is geostrophic, with the pressure gradient balancing rotation. Near the bottom, the classical Ekman balance between the pressure gradient, rotation, and vertical diffusion holds (no contours are visible near the bottom in Figure 12, however, because of the small magnitude of the near-bottom terms relative to those near the surface). The same balances also hold in the y direction, with Ekman balances near

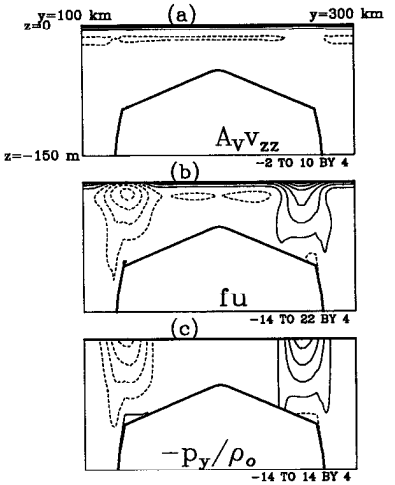

Figure 12. The v momentum terms along $x = 200$ km after 3 days of moderate wind forcing. The vertical diffusion term $A_V v_{zz}$ appears in (a), the Coriolis term $-fu$ appears in (b), and the pressure gradient term $-(1/\rho_o)\,\partial p/\partial y$ appears in (c). The contoured values are in units of m $s^{-2} \times 10^{-6}$.

the surface and bottom and a geostrophic balance in the interior. For the density equation, (5), the primary balance near the surface is between time dependence and advection, i.e. the density field never reaches a quasi-steady state while the wind stress is present. The balances described here for the momentum and density equations also hold for strong wind forcing, but the effect of diffusion and rotation relative to the pressure gradient is much greater within the region of the frontal outcrop.

While the cases described here have been limited to a synoptic meteorological scale, runs of longer duration show similar effects. A longer run using a periodic channel revealed that the advection of light bank water off the bank in the Ekman loss region of the bank continued, while the density gradient area on the Ekman gain region of the bank continued to be displaced on bank. After 20 days of wind forcing with a 1 dyne cm^{-2} wind, the inner edge of the density gradient region on the Ekman gain side of the bank was nearly in the center of the bank.

5. Wind cessation

Strong wind forcing events in the Georges Bank region are typically 1 to 3 days in duration, so it is important to consider the response of the flow field when the wind forcing is abruptly turned off and the fate of the light bank water which is advected off the bank. While the azimuthal flow is restored rapidly, on the order of an inertial period, little of the near-surface bank water removed from the bank is restored to the bank.

This is demonstrated most clearly in the case with strong wind forcing. The surface velocity field three days after the wind has been turned off (Fig. 13) shows that the anti-cyclonic around-bank circulation is mostly restored, although the flow on the Ekman loss side of the bank is both broader and more sluggish than the initial geostrophically-adjusted field. The flow on the Ekman gain side of the bank is still displaced onto the bank relative to its position prior to the start of the wind forcing. The time evolution of the surface and mid-depth velocity at the point $x = 200$ km, $y = 133$ km is shown in Figure 14 for both the wind forcing and cessation periods (days 10–16). The along-bank velocity (u) at the surface is restored to a value close to the unforced value over the time scale of an inertial period, although inertial waves are still present three days after wind cessation. Thus, the anti-cyclonic surface flow is restored on a time scale of f^{-1}, although it reaches a value of only 0.11 m s^{-1} three days after wind cessation versus the original value of 0.16 m s^{-1} immediately before the wind forcing began. At mid-depth ($z = -45$ m), there is not a major change in the velocity when the wind is turned off because it is much deeper than the surface Ekman layer.

A plan view of the surface density field shows that a significant amount of light fluid is still off of the bank three days after wind cessation (Fig. 15). The area of light fluid off the bank has contracted relative to that after three days of wind forcing

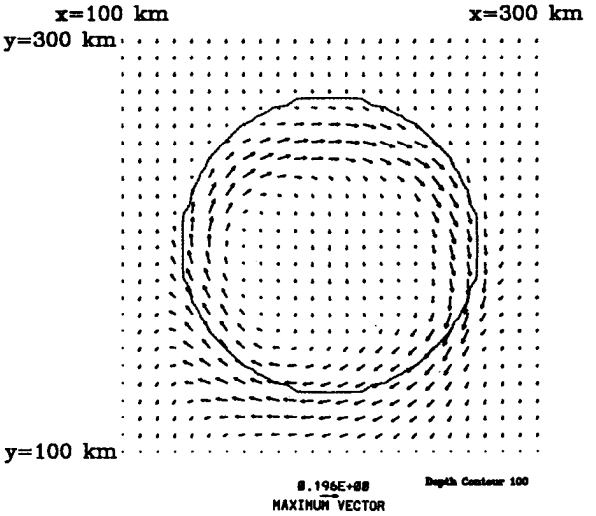

Figure 13. A plan view of the surface velocity field after 3 days of strong wind forcing and 3 days with no wind forcing.

(Fig. 8b), but this is due to both the readjustment of the density field and diffusive mixing of the near-surface water with underlying water. The time scale for vertical mixing is

$$t_m \approx \frac{\Delta z^2}{A_V}. \tag{14}$$

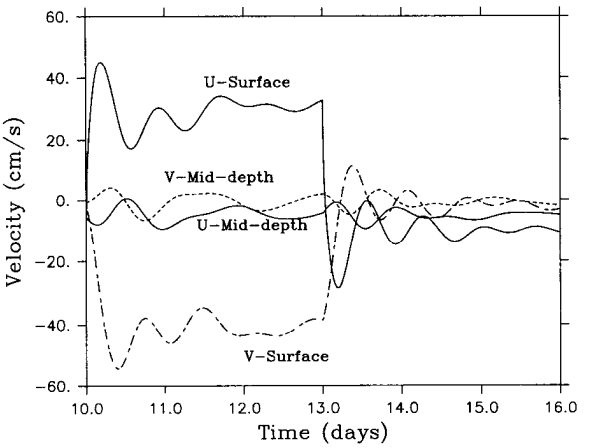

Figure 14. The time-dependent behavior of the velocity field at x = 200 km, y = 133 km (r = 67 km) for three days of strong wind forcing and three days with no wind forcing. The u and v velocities are shown at the surface and mid-depth.

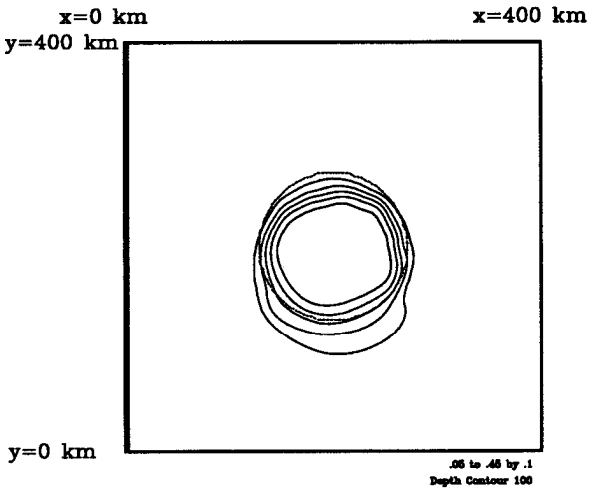

Figure 15. A plan view of the surface perturbation density field after 3 days of strong wind forcing and 3 days with no wind forcing.

For $\Delta z = \delta_E = 10$ m and $A_v = 0.005$ m^2 s^{-1}, the time scale for mixing is 0.23 days, and so light water present in the Ekman layer would diffuse away fairly rapidly after the wind stops. This points out the difficulty of using density to track the advection of the bank water mass: vertical mixing may rapidly eradicate the identity of the initial bank water advected off of the bank. For this reason, neutrally-buoyant particles are used in the next section to estimate the volume of water lost from the bank.

6. Lagrangian flow behavior and bank losses

The motions of neutrally-buoyant particles within the flow fields described in Sections 4 and 5 are useful in clarifying the advective losses from the bank associated with wind forcing. The motion of particles will be described for days 10–16, i.e. through three days of wind forcing and three days without wind forcing. The particle trajectories are calculated using a fourth order Runge-Kutta scheme described by Hedstrom (1990). A bilinear interpolation scheme which uses the four neighboring grid points is used to interpolate the velocity field at the position of the particle.

One would expect that the fates of particles initialized in different regions of the bank would be quite different. Figure 16 shows the six day trajectories of neutrally-buoyant particles initialized at a depth of 5 m (i.e. within the surface Ekman layer) for strong wind forcing. Virtually all of the particles are lost from the bank except on the Ekman gain side where only a few of the particles are lost (Fig. 16b). Particles are carried farthest off the bank from the Ekman loss and downwind regions of the bank (Figs. 16a and 16d).

Another way to consider the particle behavior is to view the areas from which the near-surface particles are lost from the bank. Figure 17a shows the area where

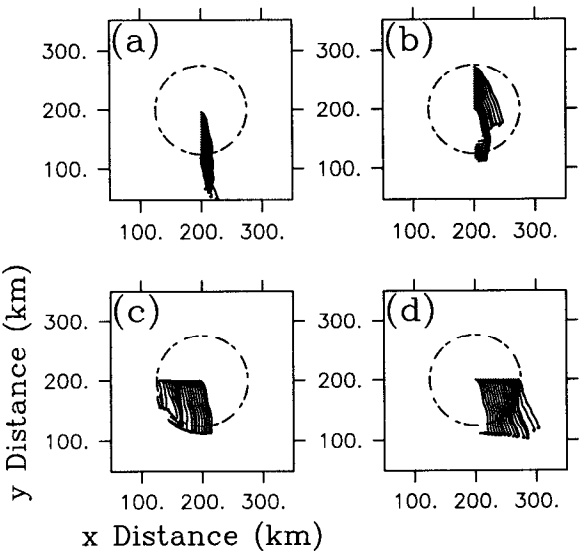

Figure 16. The 6 day trajectories of neutrally-buoyant particles initialized at a depth of 5 m. A wind stress of 4 dynes cm^{-2} is applied for 3 days and and is turned off for 3 days. The Ekman loss and Ekman gain regions appear in (a) and (b) while the upwind and downwind regions appear in (c) and (d). The wind stress is applied from left to right in this figure.

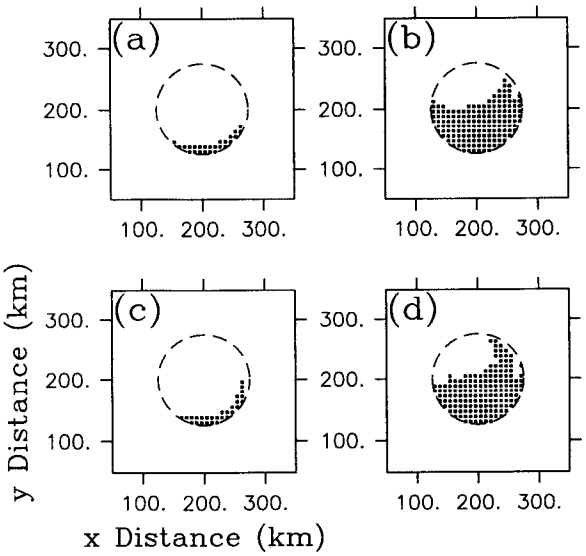

Figure 17. The initial locations of particles which leave the bank after 3 days of wind forcing. The distribution appears in (a) for $\Delta\rho = 0$ (i.e. no density front) and 1 dyne cm^{-2}, and in (b) for $\Delta\rho = 0$ and 4 dynes cm^{-2}. The distribution appears in (c) for $\Delta\rho = 0.5$ kg m^{-3} and 1 dyne cm^{-2}, and in (d) for $\Delta\rho = 0.5$ kg m^{-3} and 4 dynes cm^{-2}.

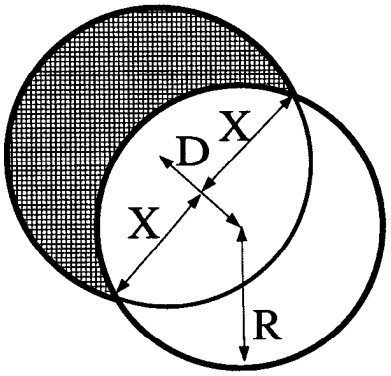

Figure 18. A plan view of the geometry of Eq. (15), the simple estimate for particle loss from a circular region. The radius is R. The translation distance due to the wind forcing is D. The shaded area indicates the region where particles have been removed from the bank.

particles initialized at a depth of 5 m have been advected off the bank by three days of a 1 dyne cm^{-2} wind stress in the absence of a buoyancy-driven flow ($\Delta\rho = 0$). The near-surface particles are lost, as one would expect, from a thin crescent centered between the downwind and Ekman loss sides of the bank; 19% of the particles are lost. For the stronger wind stress of 4 dynes cm^{-2} (Fig. 17b), 70% of the particles are lost.

The addition of the density-driven flow does not substantially change the number of near-surface particles lost from the bank. Figures 17c,d show the location of particles lost for the flows with moderate wind forcing described in Section 4. Fewer particles are lost on the upwind side of the bank, where there was a minimum in the surface velocity (Fig. 5), whereas more particles are lost along the crescent extending into the Ekman gain side of the bank where the surface velocities are enhanced. For the moderate wind forcing, 23% of the particles at 5 m depth are lost, while 73% of the particles are lost for the strong wind forcing. Thus, the strength of the wind forcing is critical in determining the amount of near-surface particle loss, while the density front primarily alters the location of the particle losses.

The amount of particles lost decays with depth, but is still evident at a depth of 15 m. For moderate wind forcing, 12% of the particles at 10 m are lost and 6% of the particles at 15 m are lost. For strong wind forcing, 39% of the particles at 10 m and 23% at 15 m are lost.

The dependence of the particle losses on the wind strength can be estimated by considering wind forcing over a circular region lacking any density-driven flow. Assuming a constant, spatially uniform wind stress, the particles at a given depth within the circular region are advected a uniform distance $D = t\,u(z)$, where t is the time, and $u(z)$ is the depth-dependent velocity (Fig. 18). The percentage of particles

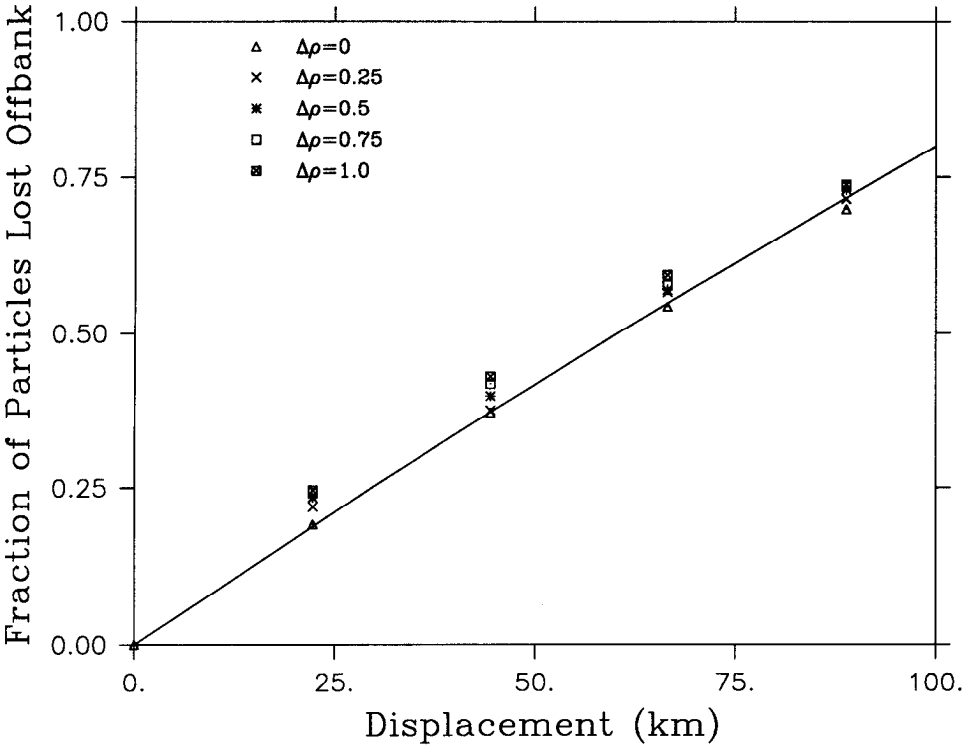

Figure 19. The percentage of particles initialized at a depth of 5 m removed from the bank after 3 days of wind forcing as a function of displacement and initial density difference. The solid line is the value from Eq. (15) and the symbols are values calculated for the model runs, in which the initial density difference was varied from 0 to 1.0 kg m^{-3}. The four displacements with the variable density differences correspond to three days of wind forcing at 1, 2, 3, and 4 dynes cm^{-2} at a depth of 5 m with $A_V = 0.0050\ m^2\ s^{-1}$.

P lost from the circular region is

$$P = 1 - 2\left[\left(\frac{\tan^{-1}(2X/D)}{\pi}\right) - \left(\frac{XD}{2\pi R^2}\right)\right] \tag{15}$$

where R is the radius, and $X = \sqrt{R^2 - (D^2/4)}$.

Figure 19 compares the simple formula (15) with the percentage of particles initialized at a depth of 5 m and subsequently lost from the bank for various displacements and initial density differences based on numerical calculations using a constant value for the vertical mixing coefficient of 0.0050 $m^2\ s^{-1}$. The agreement between (15) and the results from the primitive equation model is quite good. More importantly, however, Figure 19 shows that the particle losses are relatively insensitive to the initial density difference across the front at the edge of the bank, with only a slight increase in particle losses as the density difference is increased.

The volumetric losses of water from the bank can be estimated by multiplying the percentage particle loss at a given depth by the bank area and a representative thickness for that depth. The thicknesses are taken to be 7.5 m for the particles initialized at 5 m, and 5 m for the particles initialized at 10 m and 15 m. For moderate wind forcing, the volumetric loss is 4.6×10^{10} m^3, or 3.5% of the total bank volume (13.3×10^{12} m^3). For strong wind forcing, the volumetric loss is 15.2×10^{10} m^3, or 11% of the total bank volume. These estimates are both comparable to the Ekman transport, which is 3.9×10^{10} m^3 and 15.6×10^{10} m^3 for the two cases, respectively.

These results suggest several conclusions. First, particle losses are concentrated in the near-surface region on the order of the Ekman decay scale in the vertical. Secondly, the loss regions are localized, and near surface particles in the "stagnation" region near the upwind side of the bank are virtually motionless during the wind forcing for the case of moderate wind forcing. Thus localized losses may be quite high in the surface region between the downwind and Ekman loss sides of the bank while there are virtually no losses anywhere else near the surface at moderate wind forcing. Finally, because this is a circular bank, the response is independent of the wind direction.

7. Discussion

Despite the highly idealized nature of this study, there are several results that should be robust. The first is the strong asymmetry of the surface velocity field due to the changing orientation of the density-driven flow relative to the wind-driven flow. This was particularly important in defining regions in which near-surface particles are lost from the bank. The upwind side of the bank, in which the two flow components are opposed, is virtually a stagnant region when the flows are of comparable strength and few particles are lost from this region. On the downwind side of the bank, the two flow components are aligned in the same direction and there are large particle losses in this region. Thus, the wind forcing can have very different effects on different portions of the bank. There is some observational evidence consistent with the superposition of the wind and buoyancy-driven flows in the surface drifter observations of Frye (1979) during the winter of 1978. He noted that drifters over the south flank of Georges Bank behaved in a manner indicative of a combination of the along-isobath density-driven flow and the wind-driven component.

Secondly, the rapid restoration of the around-bank flow near the surface within an inertial period after the wind ceased is consistent with observations that show the anti-cyclonic gyre over Georges Bank to be very robust and not disrupted by strong winter wind forcing (Butman, 1987). The model results also show that the advective loss of particles from the bank is limited to the near surface region directly influenced by the wind forcing, and particles in the underlying water column are not removed from the bank. (In reality, turbulent fluctuations due to high-frequency processes not

resolved in this model would tend to randomly distribute particles vertically throughout the water column and thus in and out of the surface well-mixed layer.)

Third, the tendency of particles advected off the bank to remain off the bank and not return to the bank circulation has been observed by Beardsley *et al:* (1991) using drifters drogued at 5 m in SCOPEX (South Channel Ocean Productivity Experiment). Four of the drifters originally deployed during the summer were still present on the south flank of Georges Bank during the winter, and were advected off the bank during strong wind forcing events. In each case, the drifters did not return to the bank but were eventually advected southward to the Gulf Stream.

Finally, the presence of the density front does not inhibit advective losses near the surface. The ease with which light surface water is advected out of the region in the surface Ekman layer may account for the frequent observations of low salinity water near the surface in the slope region (Lyne and Csanady, 1984).

There are many highly idealized aspects of this study which preclude a more detailed comparison with observations in regions such as Georges Bank. The most obvious is the use of a constant vertical mixing coefficient. It has long been established (e.g. Gregg, 1987) that the vertical mixing in the ocean is dependent on the stratification. In addition, in regions with large tidal flows such as Georges Bank, the tidal motions can dramatically increase the vertical mixing over the bank (e.g. Chen, 1992). Each of these effects was neglected in order to examine simple dynamics.

Several tests were performed using the parameterization for the vertical mixing coefficients of James (1977) which includes the effect of a variable Richardson number, and the results were not sensitive to this parameterization. An unrealistic aspect to the vertical mixing coefficient is the lack of a dependence on $u_* = \sqrt{\tau/\rho}$. The vertical mixing in the surface mixed layer has been commonly scaled by u_* (e.g. Stull, 1988; Santiago-Mandujano and Firing, 1990), and so the comparisons in Figure 19 are artificial in the sense that the vertical mixing coefficients are deliberately held constant. As the surface stress is increased, the vertical mixing coefficient should increase so that the momentum is mixed more deeply into the water column. This would have the effect of decreasing the particle losses near the surface and increasing the particle losses at greater depths relative to the results presented in Section 6. There is a variety of parameterizations that could be chosen, and future work should include the use of a sophisticated surface mixed layer scheme such as the Price *et al.* (1986) scheme or a turbulence closure scheme.

The effects of surface buoyancy forcing have also not been included. Adamec and Garwood (1986) have shown that buoyancy forcing can have a significant effect on frontal structure in a two-dimensional model, and this should be included in future work. The use of a more sophisticated initial frontal condition, as opposed to the geostrophically-adjusted flow, would also make the results more realistic.

8. Conclusions

A primitive equation numerical model has been used to study the response of a bank-trapped density front to spatially-uniform, steady wind forcing. The initial density-driven flow results from the geostrophic adjustment of a quiescent, vertically-uniform cylinder of relatively light water centered on a circular bank. The resulting flow is anti-cyclonic at the surface and cyclonic near the bottom. Bottom friction makes the cyclonic bottom flow much weaker than the surface flow.

When a steady, spatially-uniform wind stress is applied over the domain, the response is basically a superposition of the wind-driven flow and the density-driven flow near the surface, such that the surface flow is a maximum on the downwind side of the bank, where the flows are in the same direction, and a relative minimum on the upwind side of the bank, where the flows are in opposite directions. In the region where Ekman transport is off of the bank, light bank water is advected off the bank and remains off the bank when the wind forcing ceases. The near-surface density gradients are weakened in this region due to the wind-driven advection, which is the primary nonlinear mechanism evident in the flow field. In the region where Ekman transport is onto the bank, the density front is rapidly mixed vertically due to advection of dense water into the frontal region with subsequent convective mixing, and the front is slowly advected onto the bank. After the wind forcing is abruptly turned off, the around bank flow is re-established near the surface within one inertial period. Neutrally-buoyant particles are lost from the bank primarily in the near-surface region directly affected by the wind forcing. The presence of the density front does not inhibit wind-driven advection off the bank.

Acknowledgments. I thank D. Chapman and S. Lentz for many fruitful conversations about the course and interpretation of this work. Discussions with R. Beardsley on the SCOPEX drifters were very helpful. The contribution of D. Haidvogel and K. Hedstrom in assisting with model issues is also appreciated. I thank R. X. Huang for a helpful discussion on Eq. (15). I appreciate the assistance of an anonymous reviewer and the editor. Financial support was provided by the National Science Foundation under Grant OCE90-16893 as part of the GLOBEC Initiative. Computer facilities at the National Center for Atmospheric Research in Boulder, Colorado, were used for the numerical calculations. NCAR is funded by the National Science Foundation. This is contribution number 8141 of the Woods Hole Oceanographic Institution.

REFERENCES

Adamec, D. and R. W. Garwood, Jr. 1986. The simulated response of an upper-ocean density front to local atmospheric forcing. J. Geophys. Res., *90,* C1, 917–928.

Beardsley, R. C., R. Limeburner and C. Chen. 1991. Summertime Lagrangian circulation in the Great South Channel/Georges Bank region. EOS, Trans. AGU, *72,* 260.

Brink, K. H. 1983. Low-frequency free wave and wind-driven motions over a submarine bank. J. Phys. Oceanogr., *13,* 103–116.

Butman, B. 1987. Physical processes causing surficial sediment movement, *in* Georges Bank, R. Backus, ed., MIT Press, Cambridge, MA, 147–162.

Chao, S.-Y. 1988. Wind-driven motion of estuarine plumes. J. Phys. Oceanogr., *18,* 1144–1166.

Chen, C. 1992. Variability of currents in Great South Channel and Georges Bank: Observation and modelling. Ph.D. Thesis, W.H.O.I./M.I.T. Joint Program in Oceanography, Woods Hole, MA, 277 pp.

Csanady, G. T. 1978. Wind effects on surface to bottom fronts. J. Geophys. Res., *83,* C9, 4633–4640.

—— 1984. The influence of wind stress and river runoff on a shelf-sea front. J. Phys. Oceanogr., *14,* 1383–1392.

Dewar, W. K. and P. D. Killworth. 1990. On the cylinder collapse problem, mixing, and the merger of two isolated eddies. J. Phys. Oceanogr., *20,* 1563–1575.

Frye, D. (Principal Author), 1979. Data report, Lagrangian studies Dec. 1978–Mar. 1979, App. A 10th quarterly progress report, New England Outer Continental Shelf Physical Oceanography Program. EG&G Environmental Consultants, Waltham MA, 32 pp.

GLOBEC. 1992. Northwest Atlantic Implementation Plan. U.S. Global Ocean Ecosystem Dynamics Report Number 6, 69 pp.

Gregg, M. C. 1987. Diapycnal mixing in the thermocline: a review. J. Geophys. Res., *92,* C5, 5249–5286.

Haidvogel, D., J. Wilkin and R. Young. 1991. A semi-spectral primitive equation ocean circulation model using vertical sigma and orthogonal curvilinear horizontal coordinates. J. Comp. Physics, *94,* 151–185.

Hedstrom, K. 1990. User's manual for a semi-spectral primitive equation regional ocean-circulation model version 3.0 B. Technical report SR-1, Institute for Naval Oceanography, 82 pp.

Ikeda, M. 1985. Wind effects on a front over the continental shelf slope. J. Geophys. Res., *90,* C5, 9108–9118.

James, I. D. 1977. A model of the annual cycle of temperature in a frontal region of the Celtic Sea. Estuar. Coastal Mar. Sci., *5,* 339–353.

Killworth, P. 1992. The time-dependent collapse of a rotating fluid cylinder. J. Phys. Oceanogr., *22,* 390–397.

Klein, P. 1987. A simulation of some physical and biological interactions, *in* Georges Bank, R. Backus, ed., MIT Press, Cambridge, MA, 395–405.

Loder, J. W., C. K. Ross and P. C. Smith. 1988. A space- and time-scale characterization of circulation and mixing over submarine banks, with application to the northwestern Atlantic continental shelf. Can. J. Fish. Aquat. Sci., *45,* 1860–1885.

Lyne, V. D. and G. T. Csanady. 1984. A compilation and description of hydrographic transects of the Mid-Atlantic Bight shelf-break front. Woods Hole Oceanographic Institution Technical Report WHOI-84-19, 290 pp.

Ou, H. W. 1983. Some two-layer models of the shelf-slope front: Geostrophic adjustment and its maintenance. J. Phys. Oceanogr., *13,* 1798–1808.

—— 1984a. Wind-driven motion near a shelf-slope front. J. Phys. Oceanogr., *14,* 985–993.

—— 1984b. Geostrophic adjustment: A mechanism for frontogenesis. J. Phys. Oceanogr., *14,* 994–1000.

Price, J. F., R. A. Weller and R. Pinkel. 1986. Diurnal cycling: observations and models of the upper ocean response to diurnal heating, cooling, and wind mixing. J. Geophys. Res., *91,* C6, 8411–8427.

Santiago-Mandujano, F. and E. Firing. 1990. Mixed-layer shear generated by wind stress in the central equatorial Pacific. J. Phys. Oceanogr., *20,* 1576–1582.

Stull, R. B. 1988. An Introduction to Boundary Layer Meteorology, Kluwer Academic Publishers, Boston, MA, 666 pp.

Walsh, J. J., T. E. Whitledge, J. E. O'Reilly, W. H. Phoel and A. F. Draxlers. 1987. Nutrient cycling on Georges Bank and the New York shelf: A comparison between well-mixed and seasonally stratified waters, *in* Georges Bank, R. Backus, ed., MIT Press, Cambridge, MA, 234–246.

Wang, D.-P. 1984. Mutual intrusion of a gravity current and density front formation. J. Phys. Oceanogr., *14,* 1191–1199.

Received: *15 September, 1992;* revised: *3 December, 1992.*